NANO LETTERS
Letter
pubs.acs.org/NanoLett

How Graphene Slides: Measurement and Theory of Strain-Dependent Frictional Forces between Graphene and SiO_2

Alexander L. Kitt,[†] Zenan Qi,[‡] Sebastian Rémi,[†] Harold S. Park,[‡] Anna K. Swan,[§,†,∥] and Bennett B. Goldberg*[,†,⊥,∥]

[†]Department of Physics, Boston University, 590 Commonwealth Avenue, Boston, Massachusetts 02215, United States
[‡]Department of Mechanical Engineering, Boston University, 110 Cummington Mall, Boston, Massachusetts 02215, United States
[§]Department of Electrical and Computer Engineering, [∥]Photonics Center, and [⊥]Center for Nanoscience and Nanobiotechnology, Boston University, 8 St Mary's Street, Boston, Massachusetts 02215, United States

Supporting Information

ABSTRACT: Strain, bending rigidity, and adhesion are interwoven in determining how graphene responds when pulled across a substrate. Using Raman spectroscopy of circular, graphene-sealed microchambers under variable external pressure, we demonstrate that graphene is not firmly anchored to the substrate when pulled. Instead, as the suspended graphene is pushed into the chamber under pressure, the supported graphene outside the microchamber is stretched and slides, pulling in an annulus. Analyzing Raman G band line scans with a continuum model extended to include sliding, we extract the pressure dependent sliding friction between the SiO_2 substrate and mono-, bi-, and trilayer graphene. The sliding friction for trilayer graphene is directly proportional to the applied load, but the friction for monolayer and bilayer graphene is inversely proportional to the strain in the graphene, which is in violation of Amontons' law. We attribute this behavior to the high surface conformation enabled by the low bending rigidity and strong adhesion of few layer graphene.

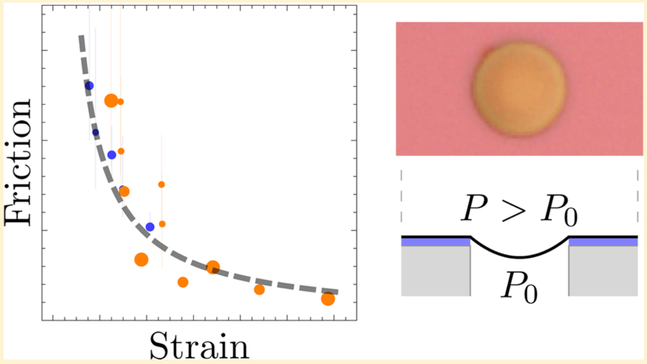

KEYWORDS: *Graphene, strain, friction, Raman spectroscopy, bilayer graphene, tribology*

Graphene is an amazing mechanical system with extreme elasticity,[1] ultrastrong adhesion,[2] and impermeability to gases.[3] As a pure two-dimensional material, graphene's interactions with its supporting substrate are unique. Amontons' first law states that macroscopic friction is proportional to the applied load, justified by arguing that increasing the load increases the microscopic contact area between two surfaces.[4] Graphene, however, because of its ultrastrong adhesion[2] and low bending rigidity requires no load to achieve nearly perfect conformation to the nanoscale topography of its substrate, especially the commonly used SiO_2.[5−7] Hence, the friction between graphene and SiO_2 might be expected to exhibit an atypical load dependence. The ability to control the thickness of few layer graphene (FLG) at an atomic scale makes it an excellent model system to study the role of thickness and load on friction, which has not previously been quantified or elucidated in detail. To date most tribological studies of FLG and graphitic materials have measured the interaction between graphene and a scanning probe tip using frictional force microscopy.[8−14] These nanoscale measurements have shown interesting effects such as superlubricity in graphite,[8] negative frictional coefficient for chemically modified graphite,[9] and increasing friction with decreasing FLG thickness.[10−13] Both the negative frictional coefficient and the increasing friction with decreasing thickness have been attributed to the puckering of graphene about the scanning probe tip.[9−11]

Here, for the first time we directly measure the intrinsic sliding of graphene over a SiO_2 substrate at the macroscopic device scale and, further, extract both the load and atomic layer dependence of sliding friction or the substrate's resistance to graphene sliding. We isolate the graphene−substrate interaction and avoid introducing a scanning probe tip to the system by using variable gas pressure applied to an FLG sealed microchamber as shown in Figure 1. The pressure acts as a tunable load, simultaneously pressing the supported graphene into the substrate while forcing the suspended FLG into the microchamber. In situ Raman measurements, which can easily measure FLG extensions of 1 nm over 1 μm, show that an annulus of the supported FLG reproducibly slides toward the center of the microchamber. By analyzing the strain response with a newly derived extension of the continuum Hencky

Received: February 25, 2013
Revised: April 10, 2013
Published: April 29, 2013

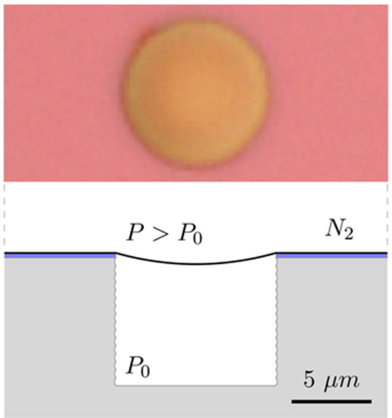

Figure 1. Top: An optical image of a trilayer graphene-sealed microchamber. Bottom: Device cross-section schematic showing the microchamber etched 8 μm into the underlying Si substrate and the supported graphene atop the 300 nm of thermal oxide. Pictured to scale is the largest pressure-induced deflection of the graphene achieved in any of the analyzed experiments.

model, we are able to extract load-dependent sliding frictions for mono-, bi-, and trilayer graphene. The layer dependence exhibits a crossover between bilayer and trilayer; the trilayer sliding friction obeys Amontons' first law, whereas the monolayer and bilayer sliding friction uniquely scales with the inverse of the strain in the graphene. We attribute these interesting results to the interplay between adhesion, in-plane strain and bending rigidity in this two-dimensional tribological system. A firm understanding of graphene's sliding friction is necessary for a variety of exciting graphene devices such as flexible bistable displays,[15] graphene electro-mechanical switches,[16] strain-engineered devices[17] that take advantage of strain-induced vector-potentials and pseudomagnetic fields,[18−20] and high quality factor graphene mechanical resonators.[21−24]

Micro-Raman spectroscopy is a powerful tool to measure strain distributions in graphene. The Raman G band measures the zone center, in-plane optical phonons that are degenerate at zero strain. In the absence of shear strain, the G band shifts according to[25]

$$\Delta\omega_G = -\omega_0\gamma(\varepsilon_r + \varepsilon_t) \pm \frac{1}{2}\beta(\varepsilon_r - \varepsilon_t) \tag{1}$$

where ε_r and ε_t are the strain in the radial and tangential directions, γ is the Grüneisen parameter, and β is the shear deformation potential that details the amount of splitting between the G^+ and G^- bands. Light scattered by the G^+ and G^- bands has orthogonal linear polarizations.[25]

A cross-section of one of our microchambers sealed with mechanically exfoliated FLG is depicted in Figure 1 (for fabrication details see the Supporting Information). The large microchamber depth of ∼8 μm is 10 times the largest FLG deflection of 700 nm, allowing us to both ignore changes in internal pressure as the applied pressure is increased and to measure for longer times because of slower leak-out rates through the silicon substrate. To eliminate surface residues, the substrate was oxygen plasma ashed before FLG exfoliation. It is important to note that different surface treatments may yield different sliding frictions providing a new degree of freedom in device engineering. Following exfoliation, each device was characterized using low force (≈ 1 nN) contact mode atomic force microscopy (AFM) as shown in Figure S1 in the Supporting Information.

The local Raman response is measured inside an optically accessible pressure chamber with a focused laser beam waist of 0.83 ± 0.01 μm while variable pressures up to 0.80 MPa are used to push the FLG into the microchamber (see Supporting Information). Unless otherwise noted, circularly polarized light is used so that the G^+ and G^- bands are measured simultaneously. A comparison of multiple linearly polarized spectra that separately measure the G^+ and G^- bands with a single circularly polarized spectra are shown in Figure S3 of the Supporting Information.

Two complementary Raman measurements are performed in situ to fully characterize the strain distributions. First, as the absolute applied pressure is varied between atmospheric pressure (0.10 MPa) and 0.80 MPa, Raman spectra at the center of the microchamber are recorded. Also, at selected pressures Raman G band line scans with 0.5 μm point spacing are taken across the microchamber. We extract the pressure inside the microchamber, P_0, from the pressure measurements at the center of the microchamber by determining the applied pressure at which the strain is minimized, as illustrated in Figure S1 of the Supporting Information for two devices.

The Raman line scans over pressurized microchambers show that the supported graphene around the microchamber has slid inward toward the center. Figure 2 shows the G band center frequency of the fit Lorentzians plotted as a function of position across a 6 μm diameter monolayer covered graphene sealed microchamber with applied absolute pressures of 0.45 and 0.80 MPa during three separate pressure cycles from atmospheric to 0.80 MPa. As expected, as the suspended graphene is pushed down into the microchamber, the G band red shifts or softens from its unstrained value. Unexpectedly, the G band of the supported graphene outside the edge of the microchamber also

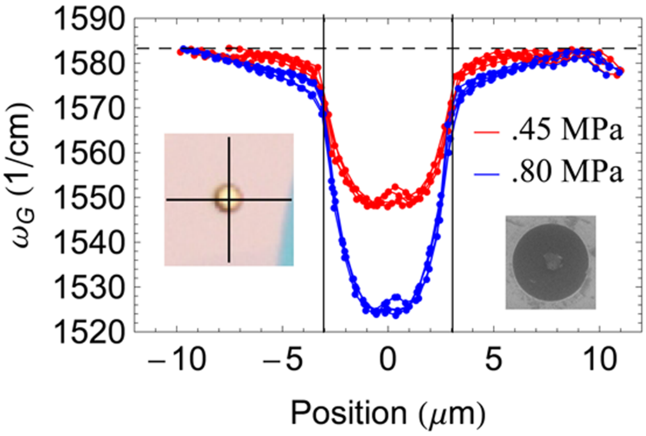

Figure 2. The frequency shift of the Raman G band as a function of position for four line scans taken at 0.45 MPa and five line scans taken at 0.80 MPa from three separate pressure cycles scanned across a single 6 μm diameter monolayer sealed microchamber. Inset left shows sample and line scan directions. Each point represents the position of the center of a single Lorentzian fit to the Raman spectra at that position. Solid vertical black lines are positioned at the edges of the microchamber and the dashed horizontal line indicates the zero strain position of the G band. Data points are separated by 0.5 μm; the focused beam has a waste of 0.81 μm. The bottom right inset is an SEM image of the device after all data acquisition showing the laser induced dirt deposited at the center of the microchamber.

shows softening, and thus significant strain. The observed softening decreases with the distance from the edge of the microchamber until the G band returns to its unstrained energy. This strain is real; the G band red shift cannot be attributed to the averaging over the finite spot size of the beam because the measured downshifts persist much further from the edge of the microchamber than the 0.83 μm beam waist. As the applied pressure increases, more strain is distributed outside of the microchamber causing both a larger redshift and a larger region over which the strain is distributed. The strain distributed outside of the microchamber's edge is a clear indicator that the graphene is not rigidly fixed to the substrate outside of the microchamber. Instead of a line force acting at the circumference of the microchamber to fix the graphene at the edge, there must be a distributed sliding frictional force, f, acting between the graphene and the substrate.

This behavior is reproducible, stable, and azimuthally symmetric. The four 0.45 MPa line scans in Figure 2 include one line scan in the x-direction for each of the first two pressure cycles and a line scan from both the x- and y-direction during the third pressure cycle. The five 0.80 MPa line scans include one line scan in the x-direction from the first pressure cycle, two sequential line scans in the x-direction which took 35 min each from the second pressure cycle, and a line scan from both the x- and y-direction during the third pressure cycle. Other than the development of a dimple at the center of the microchamber, the spectra and G band shifts are nearly identical. This dimple is the result of laser deposition of dirt at the center of microchamber due to tens of hours of high pressure resolution, single point measurements. This dirt seems to stabilize the graphene underneath, reducing the strain in its vicinity. An SEM image of the schmutz dimple is shown in the inset.

To determine the nature of the strain outside of the microchamber, Raman spectra 2 μm outside the edge of a 10 μm diameter monolayer covered microchamber were analyzed in detail. Circularly polarized spectra at this point show two discrete G^+ and G^- peaks confirmed with linearly polarized spectra as shown in Figure S4 in the Supporting Information. The peak positions indicate a tensile radial strain of 0.6% and a compressive tangential strain of −0.3% at this location. The compressive tangential strain is expected: when an annulus of the supported FLG is pulled inward, its circumference shrinks, and if the adhesion energy between FLG and its substrate is large enough to suppress out-of-plane wrinkling this shrinkage causes compressive tangential strain. In our Raman and AFM experiments, we see no evidence of the FLG wrinkling to relieve its compressive strain; as shown in Figure S5 in the Supporting Information, a partial Raman map of this 10 μm diameter monolayer covered microchamber at 0.80 MPa shows a high degree of radial symmetry indicative of wrinkle free graphene.

We have developed a continuum model to extract the sliding friction, f, from the Raman determined strain distributions. In 1915, Hencky proposed a continuum model for the nonlinear pressure induced deflection of a thin circular plate with fixed boundary conditions.[26,27] This model has been successfully used to describe a variety of systems including inflatable membrane mirrors,[28] electrostatic actuators for micro gas pumps,[29] and the topography of FLG bulging from sealed microchambers.[2] The fixed boundary conditions assumed by this model preclude its application to the strain distributions that we observe. However, we are able to relax the fixed boundary conditions and extend the Hencky model by matching the radial and tangential stresses inside the hole, derived from Hencky's model before the application of boundary conditions, to the radial and tangential stresses of the supported material outside of the hole calculated by including a sliding friction, f, acting against the radial displacement. The stresses and, using Hooke's law, the strains, are then fully determined as a function of $(\Delta P^2 E_{2D})/(f^3 R)$ where R is the radius of the microchamber measured by AFM, ΔP is the differential pressure, and E_{2D} is the 2D Young's modulus of FLG taken to be $n \times 340$ N/m where n is the number of layers.[1,2] A full derivation is included in the Supporting Information. Figure 3 compares the radial and tangential strains from the standard Hencky solution, our extended Hencky solution and an atomistic, molecular dynamics model. The solid lines of our extended model demonstrate the desired features; strain is distributed outside of the hole with compressive tangential, and tensile radial strain. The strain distribution depends on the friction as expected: at constant pressure and radius, a greater sliding friction holds the graphene more firmly to the substrate surrounding the hole, and thereby increases ε_c, the strain in the center of the microchamber while also reducing ρ_0, the largest radial distance that the strain is acting outside of the hole. Our extended model with f = 520 MPa is in good agreement with the dots in Figure 3 that are the results of an atomistic molecular dynamics simulation of a 6 nm radius microchamber under 500 MPa of pressure performed using the open source simulation package LAMMPS[30,31] developed at Sandia National Laboratories. A detailed description of the atomistic modeling is included in the Supporting Information. To our knowledge, this is the first time that Hencky's model has been generalized to allow strain to be distributed outside of the microchamber's edge.

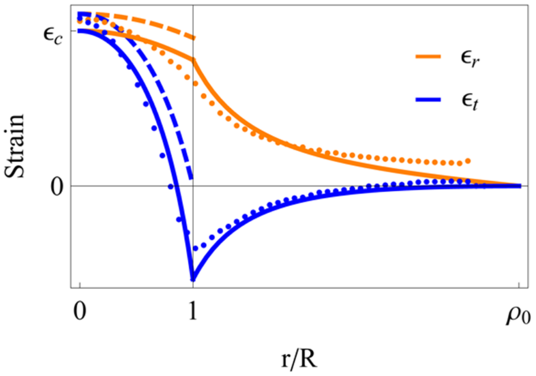

Figure 3. Theoretical strains in few-layer graphene sealed microchambers. Comparisons of the radial and tangential strains predicted by Hencky's model (dashed), our extended Hencky model that includes strain outside the microchamber for a sliding friction of f = 520 MPa (solid), and atomistic simulations of a 6 nm radius microchamber with 500 MPa of applied pressure (dots). The extended Hencky model used to extract friction agrees very well with the atomistic model.

The extended continuum model can be used to analyze the measured Raman spectra to determine the sliding friction as well as the Grüneisen parameter and shear deformation potential. Comparing the extended Hencky model to strains found by directly inverting the positions of the G^+ and G^- peaks is not possible because of the finite size of the focused laser beam. Instead, the strains predicted by the extended

Hencky model are convoluted with the system point spread function to predict an entire group of Raman G band line scan spectra for different sets of values of the fitting parameters. The set of parameters that minimize the global χ^2 is chosen as the best fit to the data. More details on the fitting as well as the approach used to estimate errors in the fitted parameters are described in the Supporting Information.

Unlike the sliding friction, the Grüneisen parameter and shear deformation potential should be the same for every line scan. As such, they were included as fitting parameters only in the two lines scans that best defined the shear deformation potential based on the splitting of the supported graphene's G band just outside the edge of the microchamber: the ~5 μm radius monolayer and the ~5 μm radius trilayer at 0.80 MPa of applied pressure. The best fit values, $\gamma = 1.89 \pm 0.01$ and $\beta = 0.70 \pm 0.04$, were then treated as known material parameters for the rest of the 20 full Raman line scans. Figure S7 in the Supporting Information details the extraction of these parameters. Table 1 summarizes the measurements of the Grüneisen parameter and shear deformation potentials of other research groups as well as their substrates. Our measured γ is commensurate with most of the other measured values and agrees particularly well with the ab initio calculations of Cheng et al.[32] On the other hand, our measured shear deformation potential is lower than most other measurements. Buckling out-of-plane cannot explain this result since the mono- and trilayers would buckle differently for a microchamber with the same pressure and radius. To our knowledge, these are the first measurements of γ and β for which the sliding of FLG over its substrate was included.

Table 1. Summary of the Grüneisen Parameter, γ, and Shear Deformation Potential, β, As Measured on Different Substrates

	γ	β
this work	1.89	0.70
SiO_2 depression[33]	2.4	
on PDMS[25]	0.69	0.38
on SU8[34]	1.99	0.99
embedded[35]	2.01	1.01
on acrylic[36]	2.2	0.93
bubble[37]	1.8	
ab initio[38]	2.0	0.66
ab initio[32]	1.86	0.96

Figure 4 shows a global data fit for an ~5 μm radius monolayer-covered graphene-sealed microchamber at 0.80 MPa of applied pressure. The spectra and fits from each position along the line scan are stacked vertically in the direction of the line scan. Our extended continuum model successfully fits the softening and splitting of the G band of the supported graphene and successfully predicts the downshift and sharpening of the G band of the suspended graphene as the center of the microchaber is approached. In comparison, without our theoretical extension the standard Hencky model would fail to reproduce the supported graphene spectra.

The sliding friction extracted for eight microchambers with radii between 1.2 and 5 μm and with applied absolute pressures from 0.10 to 0.80 MPa exhibits fundamentally different behavior for trilayer graphene than for monolayer and bilayer. In Figure 5a (left), the friction is plotted as a function of pressure and the data for trilayer graphene (black dots) shows a linear dependence of the sliding friction vs applied pressure in accordance with Amontons' law with a coefficient of friction of 0.11 ± 0.01 as shown in Figure S8 in the Supporting Information. The sliding friction for monolayer and bilayer graphene decreases generally with applied pressure and the wide scatter of the points for different radii and layer number clearly indicate that the sliding friction is dependent on the geometry of the microchamber. Our theoretical analysis shows that the radial strain at the edge due to the pressure pushing the graphene into the microchamber has the same radii and layer number dependence as the friction, so we replot the sliding friction as a function of the radial strain in Figure 5b (right). The monolayer and bilayer data for all different radii microchambers now collapse to a single curve versus radial strain, well described by $1/\varepsilon_{r,\mathrm{edge}}$ behavior (dashed line).

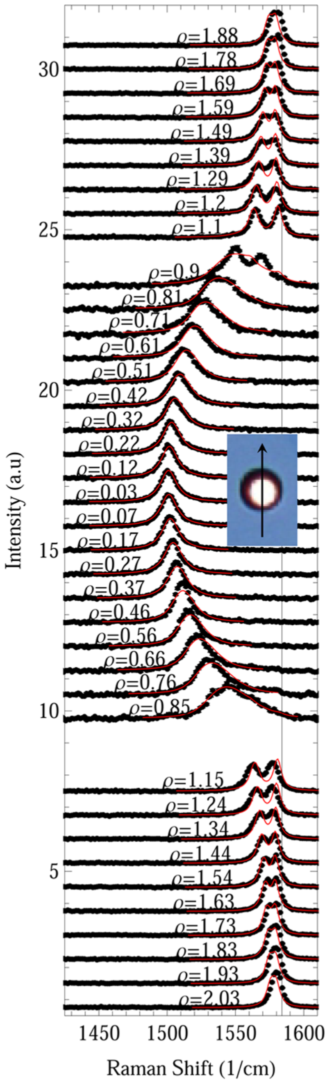

Figure 4. Raman spectra from a line scan over a ~ 5 μm radius monolayer graphene sealed microchamber with 0.80 MPa of applied pressure analyzed with our extended Hencky model (red lines). The spectra taken along the path shown in the inset are arrayed vertically with spectra taken too close to the edge of the microchamber omitted (see Supporting Information). The black vertical line is positioned at the supported graphene's unstrained G band energy.

The gross difference in behavior between trilayer on one hand, and mono and bilayer on the other, illustrates the two roles of the applied pressure. The pressure load pushes the

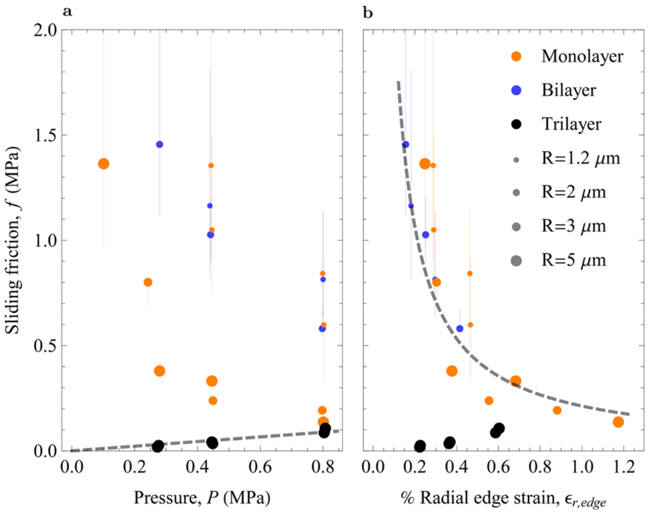

Figure 5. Sliding friction, extracted by analyzing Raman G band line scans with our extended Hencky model, plotted as a function of absolute applied pressure in panel a (left) and as a function of the radial strain at the edge of the microchamber in panel b (right) for five different graphene sealed microchambers. The size of each data point represents the radius of the FLG-sealed microchamber corresponding to that point. The error bars are given by an increase in global fit χ^2 per degree of freedom of 0.25. The sliding friction of trilayer graphene depends linearly on the absolute applied pressure in agreement with Amontons' law. The sliding friction of monolayer and bilayer graphene, however, go as the inverse of the radial strain at the edge of the microchamber. Gray dashed lines are the best fits to these trends.

graphene more firmly onto the substrate so that sliding friction should increase (Amontons' law), yielding a positive coefficient of friction. This is the case for the trilayer graphene. On the other hand, as the pressure pushes the graphene into the microchamber, it creates a radial tension in the supported graphene outside the microchamber. The data collapse in Figure 5b for monolayer and bilayer graphene demonstrate that the pressure dependence of the sliding friction is not due to loading the supported graphene but is instead due to the graphene being pulled and stretched by the applied pressure. This is the only mechanism that would depend on the geometric parameters of the microchamber while also being consistent with the data. It is not surprising that the sliding friction for mono- and bilayer graphene is dependent on the strain and not the load because thin graphene conforms nearly perfectly to a SiO_2 substrate.[5−7] Increasing the load cannot further increase the contact area, but increasing the radial strain beyond the edge of the microchamber may act to smooth out the graphene sheet, decreasing the contact between the graphene and the substrate, and thus decreasing the sliding friction. The bending rigidity, which goes as thickness cubed, of trilayer graphene must be high enough to counteract the adhesion energy, causing lower conformation and allowing for a traditional pressure and load response. The existence of a bilayer to trilayer crossover in FLG-substrate interactions is also observed in GPa range pressure measurements of silicon dioxide supported graphene.[39,40] Nicolle et al. observed a decrease in the pressure response of the G band between bilayer and trilayer graphene that was attributed to the transition from biaxial compression mediated by the substrate to hydrostatic compression mediated by the pressure transmitting medium.[40]

In summary, we have shown that graphene slides along the substrate when pulled. Furthermore, using a newly developed extension of the continuum Hencky model, we extracted the sliding friction as a function of the number of atomic layers and the load. Trilayer graphene shows a typical load response whereas the sliding friction for monolayer and bilayer graphene goes as the inverse of strain. The data collapse of the friction for mono- and bilayer graphene when plotted versus strain is strong experimental evidence for a reduction in surface conformation when graphene is pulled as the fundamental origin of the negative coefficient of friction. These results will be important for the design of strain engineered devices,[17] while the sliding of a flexible surface along a bulk object should be of fundamental, tribological interest. Finally, the method used in generalizing Hencky's solution should be useful for including distributed strains in other continuum models for use in designing strain-engineered graphene devices and in understanding other, few-layer material systems.

■ ASSOCIATED CONTENT

Ⓢ Supporting Information

Mirochamber fabrication details, ambient pressure graphene sealed microchamber behavior, Raman spectroscopy details, comparison of Raman spectra taken with circular and linear polarization, polarization-resolved Raman measurements of strained supported graphene 2 μm outside the edge of a 5 μm graphene sealed microchamber at 0.80 MPa, Raman map of 5 μm graphene sealed microchamber at 0.80 MPa, global fitting details, extraction of the Grüneisen parameter and shear deformation potential, best fit trilayer sliding friction load-dependence, derivation of the extended Hencky model, and atomistic modeling details This material is available free of charge via the Internet at http://pubs.acs.org.

■ AUTHOR INFORMATION

Corresponding Author

*E-mail: goldberg@bu.edu.

Notes

The authors declare no competing financial interest.

■ ACKNOWLEDGMENTS

We would like to thank Professor Scott Bunch for help with device fabrication. This work was supported by the Advanced Energy Consortium: http://www.beg.utexas.edu/aec/. H.S.P. and Z.Q. acknowledge support from the Mechanical Engineering department at Boston University and NSF Grant CMMI-1036460.

■ REFERENCES

(1) Lee, C.; Wei, X.; Kysar, J. W.; Hone, J. *Science* **2008**, *321*, 385−388.

(2) Koenig, S.; Boddeti, N.; Dunn, M.; Bunch, J. *Nat. Nanotechnol.* **2011**, *6*, 543−546.

(3) Bunch, J. S.; Verbridge, S. S.; Alden, J. S.; van der Zande, A. M.; Parpia, J. M.; Craighead, H. G.; McEuen, P. L. *Nano Lett.* **2008**, *8*, 2458−2462.

(4) Krim, J. *Langmuir* **1996**, *12*, 4564−4566.

(5) Stolyarova, E.; Rim, K. T.; Ryu, S.; Maultzsch, J.; Kim, P.; Brus, L. E.; Heinz, T. F.; Hybertsen, M. S.; Flynn, G. W. *Proc. Natl. Acad. Sci. U.S.A.* **2007**, *104*, 9209−9212.

(6) Lui, C.; Liu, L.; Mak, K.; Flynn, G.; Heinz, T. *Nature* **2009**, *462*, 339−341.

(7) Cullen, W. G.; Yamamoto, M.; Burson, K. M.; Chen, J. H.; Jang, C.; Li, L.; Fuhrer, M. S.; Williams, E. D. *Phys. Rev. Lett.* **2010**, *105*, 215504.

(8) Dienwiebel, M.; Verhoeven, G. S.; Pradeep, N.; Frenken, J. W. M.; Heimberg, J. A.; Zandbergen, H. W. *Phys. Rev. Lett.* **2004**, *92*, 126101.

(9) Deng, Z.; Smolyanitsky, A.; Li, Q.; Feng, X.; Cannara, R. *Nat. Mater.* **2012**, *11*, 1032−1037.

(10) Lee, C.; Li, Q.; Kalb, W.; Liu, X.-Z.; Berger, H.; Carpick, R. W.; Hone, J. *Science* **2010**, *328*, 76−80.

(11) Li, Q.; Lee, C.; Carpick, R. W.; Hone, J. *Phys. Status Solidi B* **2010**, *247*, 2909−2914.

(12) Filleter, T.; McChesney, J. L.; Bostwick, A.; Rotenberg, E.; Emtsev, K. V.; Seyller, T.; Horn, K.; Bennewitz, R. *Phys. Rev. Lett.* **2009**, *102*, 086102.

(13) Filleter, T.; Bennewitz, R. *Phys. Rev. B* **2010**, *81*, 155412.

(14) Zhang, J.; Lu, W.; Tour, J. M.; Lou, J. *Appl. Phys. Lett.* **2012**, *101*, 123104.

(15) Bonaccorso, F.; Sun, Z.; Hasan, T.; Ferrari, A. *Nat. Photonics* **2010**, *4*, 611−622.

(16) Milaninia, K. M.; Baldo, M. A.; Reina, A.; Kong, J. *Appl. Phys. Lett.* **2009**, *95*, 183105.

(17) Pereira, V. M.; Castro Neto, A. H. *Phys. Rev. Lett.* **2009**, *103*, 046801.

(18) Castro Neto, A. H.; Guinea, F.; Peres, N. M. R.; Novoselov, K. S.; Geim, A. K. *Rev. Mod. Phys.* **2009**, *81*, 109−162.

(19) Guinea, F.; Katsnelson, M.; Geim, A. *Nat. Phys.* **2009**, *6*, 30−33.

(20) Kitt, A. L.; Pereira, V. M.; Swan, A. K.; Goldberg, B. B. *Phys. Rev. B* **2012**, *85*, 115432.

(21) Kim, S. Y.; Park, H. S. *Appl. Phys. Lett.* **2009**, *94*, 101918.

(22) Bunch, J. S.; van der Zande, A. M.; Verbridge, S. S.; Frank, I. W.; Tanenbaum, D. M.; Parpia, J. M.; Craighead, H. G.; McEuen, P. L. *Science* **2007**, *315*, 490−493.

(23) Chen, C.; Rosenblatt, S.; Bolotin, K.; Kalb, W.; Kim, P.; Kymissis, I.; Stormer, H.; Heinz, T.; Hone, J. *Nat. Nanotechnol.* **2009**, *4*, 861−867.

(24) Barton, R. A.; Ilic, B.; van der Zande, A. M.; Whitney, W. S.; McEuen, P. L.; Parpia, J. M.; Craighead, H. G. *Nano Lett.* **2011**, *11*, 1232−1236.

(25) Huang, M.; Yan, H.; Chen, C.; Song, D.; Heinz, T. F.; Hone, J. *Proc. Natl. Acad. Sci. U.S.A.* **2009**, *106*, 7304−7308.

(26) Hencky, H. *Z. Math. Phys.* **1915**, *63*, 311−317.

(27) Fichter, W. *NASA Tech. Pap.* **1997**, 3658.

(28) Meinel, A. B.; Meinel, M. P. *Opt. Eng.* **2000**, *39*, 541−550.

(29) Zhang, Y.; Wang, W. *Microsystem Technologies* **2011**, *17*, 1683−1696.

(30) Lammps. http://lammps.sandia.gov, 2012.

(31) Plimpton, S. *J. Comput. Phys.* **1995**, *117*, 1−19.

(32) Cheng, Y. C.; Zhu, Z. Y.; Huang, G. S.; Schwingenschlögl, U. *Phys. Rev. B* **2011**, *83*, 115449.

(33) Metzger, C.; Rémi, S.; Liu, M.; Kusminskiy, S. V.; Castro Neto, A. H.; Swan, A. K.; Goldberg, B. B. *Nano Lett.* **2010**, *10*, 6−10.

(34) Mohiuddin, T. M. G.; Lombardo, A.; Nair, R. R.; Bonetti, A.; Savini, G.; Jalil, R.; Bonini, N.; Basko, D. M.; Galiotis, C.; Marzari, N.; Novoselov, K. S.; Geim, A. K.; Ferrari, A. C. *Phys. Rev. B* **2009**, *79*, 205433.

(35) Frank, O.; Tsoukleri, G.; Parthenios, J.; Papagelis, K.; Riaz, I.; Jalil, R.; Novoselov, K. S.; Galiotis, C. *ACS Nano* **2010**, *4*, 3131−3138.

(36) Yoon, D.; Son, Y.-W.; Cheong, H. *Phys. Rev. Lett.* **2011**, *106*, 155502.

(37) Zabel, J.; Nair, R. R.; Ott, A.; Georgiou, T.; Geim, A. K.; Novoselov, K. S.; Casiraghi, C. *Nano Lett.* **2012**, *12*, 617−621.

(38) Thomsen, C.; Reich, S.; Ordejón, P. *Phys. Rev. B* **2002**, *65*, 073403.

(39) Proctor, J. E.; Gregoryanz, E.; Novoselov, K. S.; Lotya, M.; Coleman, J. N.; Halsall, M. P. *Phys. Rev. B* **2009**, *80*, 073408.

(40) Nicolle, J.; Machon, D.; Poncharal, P.; Pierre-Louis, O.; San-Miguel, A. *Nano Lett.* **2011**, *11*, 3564−3568.